optics

MDPI

Article

Design of Double-Lattice Photonic Crystal of DUV Laser by ANN-RBF Neural Network

Bochao Zhang [1,2], Minyan Zhang [1,2,*], Lei Li [1,2], Jianglang Bie [1,2], Shuoyi Jiao [1,2], Zhuanzhuan Guo [1,2], Xinjie Cai [1,2] and Bowen Hou [1,2]

[1] Key Laboratory for Physical Electronics and Devices of the Ministry of Education & Shaanxi Provincial Key Laboratory of Photonics and Information Technology, Xi'an Jiaotong University, Xi'an 710049, China
[2] Solid-State Lighting Engineering Research Center, Xi'an Jiaotong University, Xi'an 710049, China
* Correspondence: zhangmy@xjtu.edu.cn

Abstract

In this study, a double-lattice photonic crystal structure was designed to achieve deep ultraviolet lasing without the use of any Distributed Bragg Reflector (DBR), which is called a photonic-crystal surface-emitting laser (PCSEL). The plane wave expansion (PWE) method was used to study the influence of various structural parameters on the resonant wavelength. Utilizing the random forest algorithm, we determined that the importance of the lattice constant to the resonant wavelength is 95.24%. Furthermore, we realized the reverse design of double-lattice photonic crystals from the target wavelength to optimal structural parameters through a radial basis function (RBF) network algorithm. Comparative analysis of the extreme learning machine (ELM) and back propagation (BP) algorithms demonstrated that RBF-based performance was notably superior to the training outcomes of other algorithms. The mean absolute error (MAE) of the lattice constant of the test set in the training results was 0.7610 nm, root mean square error (RMSE) was 1.143×10^{-3} nm, and mean absolute relative error (MARE) was 5.489×10^{-3}. We verified the reliability of the algorithm and designed 13 groups of photonic crystals with different epitaxial structures. The mean square error (MSE) was 0.6188 nm^2 compared with that of the plane wave expansion method. This work demonstrates applicability across various wavebands and epitaxial structures in GaN-based devices, providing a novel approach for the rapid iteration of deep ultraviolet PCSELs.

Keywords: photonic-crystal surface-emitting laser; photonic crystal; deep ultraviolet; ANN-RBF

Academic Editors: Luciana R. P. Kassab, Raul Rangel-Rojo and Rafael Salas-Montiel

Received: 24 November 2025
Revised: 26 December 2025
Accepted: 31 December 2025
Published: 2 February 2026

1. Introduction

Deep ultraviolet semiconductor lasers, with their short wavelength characteristics, have huge application prospects in nanolithography, biomolecule spectroscopic analysis, photopolymerization, and high-security communication [1]. At present, some researchers have realized solid-state edge-emitting lasers (EELs), which achieve room-temperature continuous laser emission in the 265–280 nm wavelength range through AlGaN multi-quantum-well structures [2,3]. However, they have inherent defects such as a large beam divergence angle and low system integration. Although vertical cavity surface emitting lasers (VCSELs) have theoretical advantages such as low threshold current and circular beam output [4], they are limited by the special challenges of deep ultraviolet materials. The low p-type doping efficiency of high-aluminum-component AlGaN leads to difficulties

in carrier injection, and traditional distributed Bragg reflectors (DBR) are prone to crack defects due to lattice mismatch, which seriously restricts device reliability [1]. Recently, photonic-crystal surface-emitting laser (PCSEL) has shown breakthrough potential by replacing DBR structures with two-dimensional photonic crystal resonators, fundamentally avoiding the lattice mismatch problem of heteroepitaxy [5]. By simultaneously inheriting the surface emission characteristics, a high directional laser output can be achieved without complex beam shaping, significantly improving system compactness [6].

PCSEL provides a feasible path for the miniaturization and high performance of deep ultraviolet lasers [7,8]. The Imada team realized the 1300 nm electric pump quantum well laser for the first time [9]. It used photonic crystals to form standing waves at the Dirac point at the boundary of the Brillouin zone, which enhanced the photon density of states and greatly improved the mode gain. However, traditional single-lattice PCSEL is limited by the difference in threshold gain between the fundamental and first-order modes, which severely restricts its power scaling capability. In response to this bottleneck, the academic community has focused on systematic optimization of photonic crystal structures. The team led by Cun-zhu Tong from Changchun Institute of Optics, Fine Mechanics and Physics, Chinese Academy of Science, designed the flat band structure of the photonic crystal and achieved a room-temperature continuous wave output power of 13.3 mW in the 1300 nm wavelength band [10]. Meanwhile, the Noda team at Kyoto University proposed a double-lattice photonic crystal structure [11]. By introducing a 1/4 wavelength shift in the x/y direction between two photonic crystal lattice groups in the photonic crystal, the threshold gain difference between the fundamental and higher-order modes was effectively increased, enabling a 500 μm diameter device to achieve 10W single-mode output. The Ren-min Ma team at Peking University achieved stable operation at room-temperature with a threshold of kilowatts per square centimeter by introducing a topological cavity structure, with a single-mode output edge mode suppression ratio exceeding 36 dB [12].

The double-lattice photonic crystal structure opens a new path for the development of a multi-material system PCSEL. According to reports, double-lattice photonic crystals have been widely used in GaN-based PCSELs (400–550 nm) [13], GaAs-based PCSELs (900–1000 nm) [11,14–17], and InP-based PCSELs (1.3 μm–1.6 μm) [18–22]. These results systematically validate the universality of the structure in the spectral range of 400 to 1600 nm, but research on double-lattice PCSEL in the deep ultraviolet band (<300 nm) is still lacking.

More importantly, the design of photonic crystal layers mostly relies on trial-and-error and the experience of researchers, which wastes a lot of computational power. With the development of artificial intelligence (AI), the method assisted by neural networks has brought new ideas to the field of photonic device design [23–25], among which, the RBF neural network has received widespread attention owing to its efficient small-sample learning ability and accurate modeling of complex nonlinear problems [26]. According to previous reports, RBF neural networks have demonstrated strong modeling capabilities in the field of integrated photonic devices [27,28].

In this study, we focused on the photonic crystal layer of PCSEL in deep ultraviolet, and systematically investigated the influence of the structural parameters of double-lattice photonic crystals on the resonant wavelength of different mode lasers. Subsequently, a training set of double-lattice structure simulation data was established, and the RBF algorithm was used to achieve an inverse design from the target wavelength to the optimal structural parameters. This method is suitable for GaN-based multi-bands and can quickly complete the matching optimization design of the photonic crystal layer for PCSEL devices with different epitaxial structures in the same band.

2. Photonic Crystal Model

The typical PCSEL structure consists of an n-cladding layer, quantum well layer, p-waveguide, p-cladding layer, and photonic crystal layer formed within it from the bottom to the top. The photonic crystal layer, constructed with a precisely engineered periodic lattice, enables two-dimensional coherent laser oscillation through coupling between first-order and high-order Bloch waves, while generating vertical diffraction output at the Γ point of the Brillouin zone in the energy bands [29,30].

Figure 1a shows the side view of the PCSEL structure used in this study. The unit cell of the double-lattice photonic crystal model is shown in Figure 1b. Usually, the distance between the two circular holes is half a cycle apart in the x- and y- directions. To facilitate the study of the influence of the relative position between the circular air holes on the resonant wavelength, we define a second relative distance d_2 and a second phase angle α_2 on the first relative distance $d_1 = \sqrt{2}a/2$ and the first phase angle $\alpha_1 = 45°$.

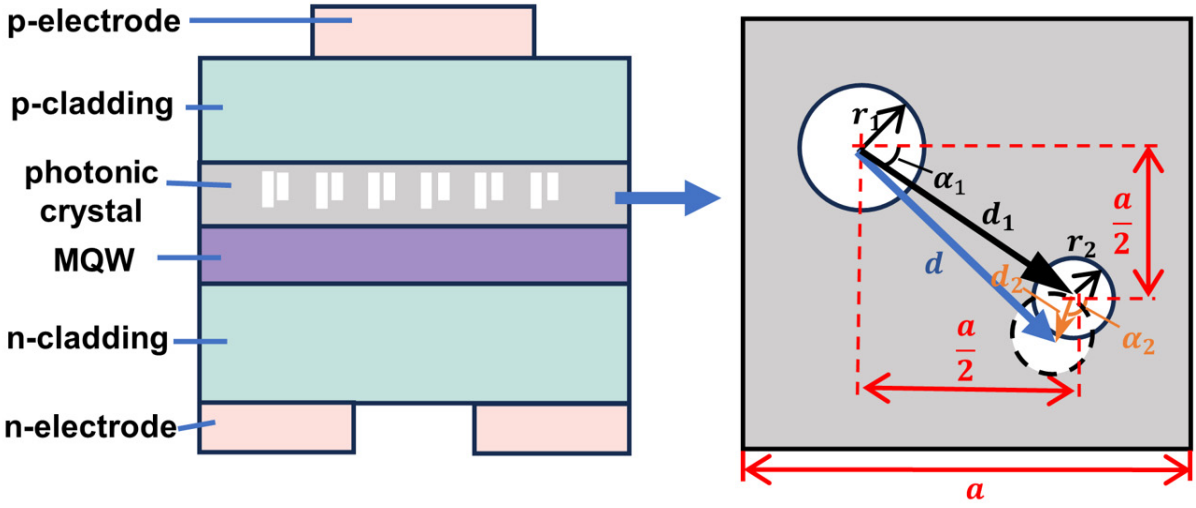

Figure 1. (**a**) Structural diagram of double-lattice photonic crystal PCSEL. (**b**) Model of double lattice photonic crystal.

The calculation results for the photonic crystal band structure determine the photonic bandgap characteristics and mode selection ability of the device near the gamma point, as shown in Figure 2. By analyzing the distribution of the band edge positions and their corresponding mode characteristics in the band diagram, we can accurately extract the resonant wavelength of the device, which can guide the structural design and optimization of photonic crystals. The mode corresponding to edge A usually has the lowest threshold and preferentially generates a laser [16,31]. Therefore, this study selected the resonant wavelength corresponding to the A mode for research. The plane-wave expansion method leverages Bloch's theorem to express the electric and magnetic fields in a photonic crystal as superpositions of plane waves. By transforming Maxwell's equations from real space into discrete Fourier space, the system is recast as an eigenvalue problem, thereby converting the computation of photonic band structures into the task of solving for eigenvalues. In this context, the plane-wave expansion method offers distinct advantages for calculating the band structures of photonic crystals. For two-dimensional photonic crystals, the governing master equation can be decoupled into two independent scalar eigenvalue equations corresponding to TE (transverse electric) and TM (transverse magnetic) polarizations, respectively. The equation is expanded into a superposition of a series of plane waves, and its eigenvalues are subsequently solved. The following formulas

represent the simplified master equations for calculating the photonic crystal's eigenvalues. By solving Equations (2) and (3) for their eigenvalues, the dispersion relation $\omega(\vec{k})$ is obtained. By varying the direction of the wave vector $\vec{k}$, the photonic band structure can then be simulated.

$$\sum_{\vec{G}_i} K(\vec{G}-\vec{G}_i)(\vec{k}+\vec{G}_i)\times\left[\left(\vec{k}+\vec{G}\right)\times\vec{E}_{\vec{k}n}\left(\vec{G}_i\right)\right]=\frac{\omega^2_{\vec{k}n}}{c^2}\vec{E}_{\vec{k}n}\vec{G} \quad (1)$$

$$\sum_{\vec{G}_i} K(\vec{G}-\vec{G}_i)(\vec{k}+\vec{G}_i)\times\left[\left(\vec{k}+\vec{G}\right)\times\vec{H}_{\vec{k}n}\left(\vec{G}_i\right)\right]=\frac{\omega^2_{\vec{k}n}}{c^2}\vec{H}_{\vec{k}n}\vec{G} \quad (2)$$

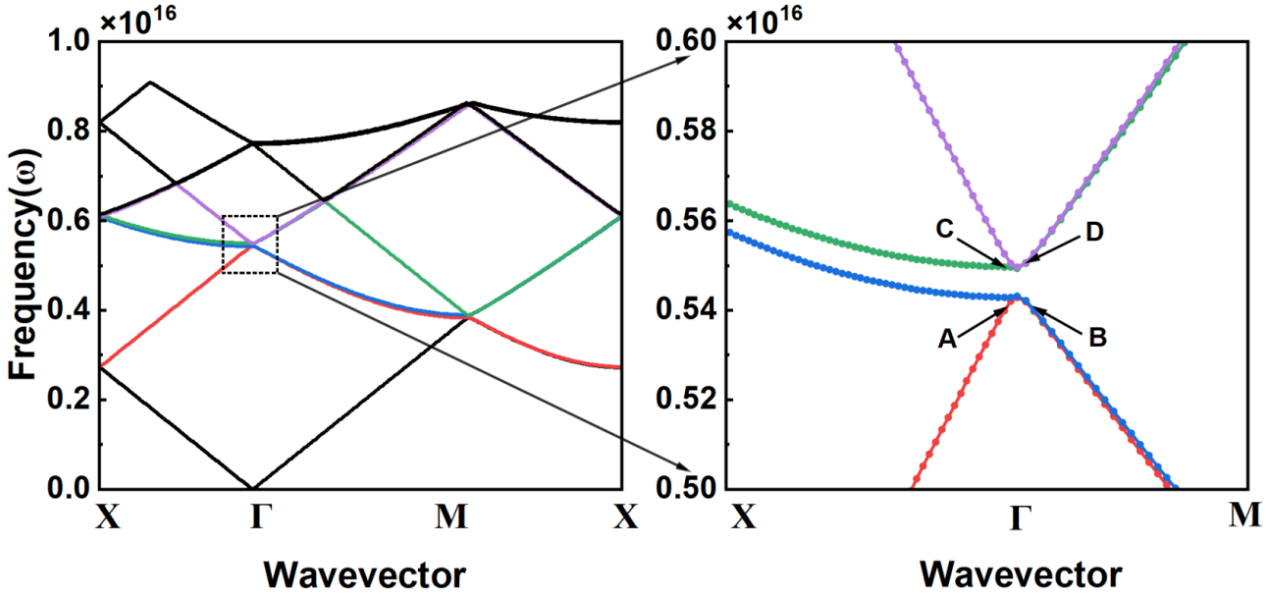

Figure 2. The band structure of photonic crystals.

The optimized plane wave expansion method is typically used to model and calculate the band structure of photonic crystal [32,33]. The dielectric constant of the modified background material is represented as ε_b, and that of the air holes is represented as ε_a. They are determined by

$$n^2_{eff} = f\varepsilon_b + (1-f)\varepsilon_a \quad (3)$$

$$\Delta\varepsilon = \varepsilon_b - \varepsilon_a = \Gamma_{pc}(\varepsilon_{\mathrm{GaN}} - \varepsilon_{air}) \quad (4)$$

where f is the area ratio of the air holes to the photonic crystal unit cell, n_{eff} is the effective refractive index, and Γ_{pc} is the confinement factor of the photonic crystal layer. Given that ε_{GaN} = 6.702 is the dielectric constant of GaN, and ε_{air} = 1 is the dielectric constant of air.

3. Results and Discussion

3.1. The Influence of Structural Factors on Resonant Wavelength

We used the random forest algorithm to calculate the degree of influence of various factors on the resonant wavelength in a double-lattice photonic crystal [34,35]. Figure 3a shows a schematic of the random forest algorithm. We used bootstrap with replacement sampling to randomly select 2000–4000 samples from the original dataset, forming a single training subset. This process was repeated 100 times to ultimately generate 100 training subsets with overlapping samples. Samples that were not selected (approximately 31.4%

of the total data) constituted the test set. To construct independent decision trees for each subset, two candidate features were randomly selected from all five features, and the optimal segmentation point was calculated within the subset based on the regression mean square error evaluation of the candidate features.

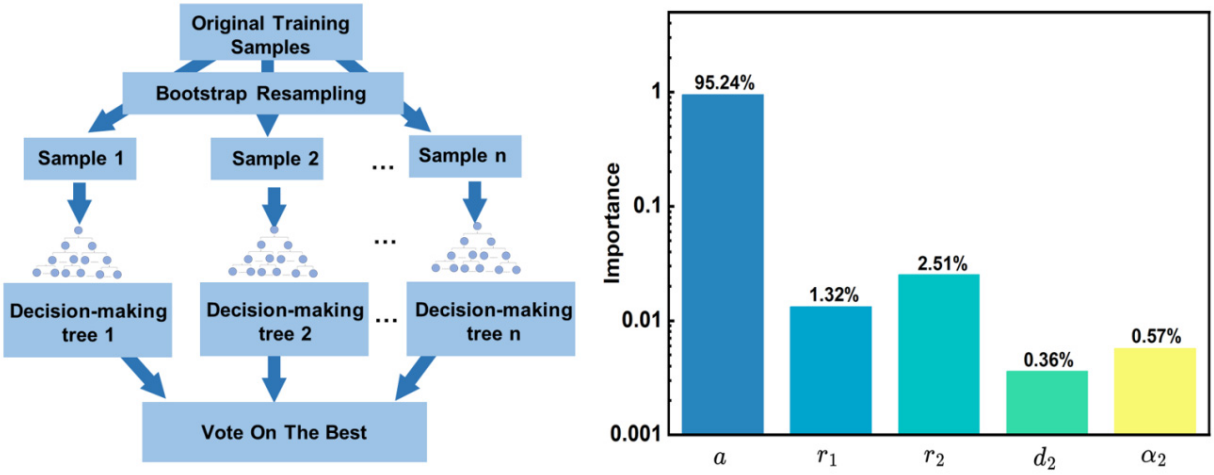

(**a**) (**b**)

Figure 3. (**a**) Schematic diagram of the random forest algorithm. (**b**) The importance of different factors.

The number of leaf nodes refers to the final number of leaf nodes in a single decision tree and directly reflects the complexity of the decision tree. Each leaf node corresponds to a prediction node [36]. After cross-validation and optimization, we adopted 1200 leaf nodes. Significant variations exist in the degree of influence of different factors on the resonant wavelength in the double-lattice photonic crystal, as shown in Figure 3b. The lattice constant has the greatest impact on the resonant wavelength, with an importance evaluation value of 95.24%, which is significantly higher than those of the other factors. The influence of the radius of the two circular air holes is secondary, with evaluation values of 1.32% (for r_1) and 2.51% (for r_2). In contrast, the influence of the second relative distance d_2 and the second phase angle α_2 on the resonant wavelength is extremely weak, with values of 0.36% and 0.57%, respectively, indicating that the contribution of these two factors to the resonant wavelength is almost negligible. Consequently, the influence of the relative position between the air holes on the resonant wavelength is excluded.

3.2. Neural Network Reverse Prediction

Firstly, we generated a dataset containing 9261 sets of structural parameters and resonance wavelength mapping relationships using the plane wave expansion method as mentioned earlier. The specific method is to traverse the radius of the two circular air holes (r_1, r_2) and the lattice constant (a) under different combinations of refractive index $(\varepsilon_a, \varepsilon_b)$. The calculated resonance wavelength of the training set data covers approximately 247–423 nm, and Table 1 shows some of the training set data. Then we trained the network to establish a forward prediction model from the photonic crystal structure to the target wavelength. As shown in Figure 4, the network structure consists of an input layer, hidden layer, and output layer. The input layer contains five neurons responsible for signal transmission $(a, r_1, r_2, \varepsilon_a, \varepsilon_b)$. The hidden layer contains 8335 radial basis function nodes using the Gaussian radial basis function as the activation function. The output layer consists of four linear neurons $(\lambda_1, \lambda_2, \lambda_3, \lambda_4)$.

Table 1. Example of the original dataset calculated by PWM.

Order Number	a (nm)	r_1(nm)	r_2(nm)	ε_a	ε_b	Resonant Wavelength Calculated by PWM (nm)
1	160	30	27	2.496	2.662	423.3118
2	152	36	27	2.496	2.662	400.8611
3	146	40	29	2.444	2.613	375.0953
4	160	30	28	2.007	2.21	350.2526
5	126	31	28	2.57	2.592	325.0331
6	142	38	29	1.942	2.151	300.019
7	130	40	29	2.098	2.125	275.0234
8	120	33	30	1.942	2.151	250.0022
9	120	40	30	1.942	2.151	247.2177

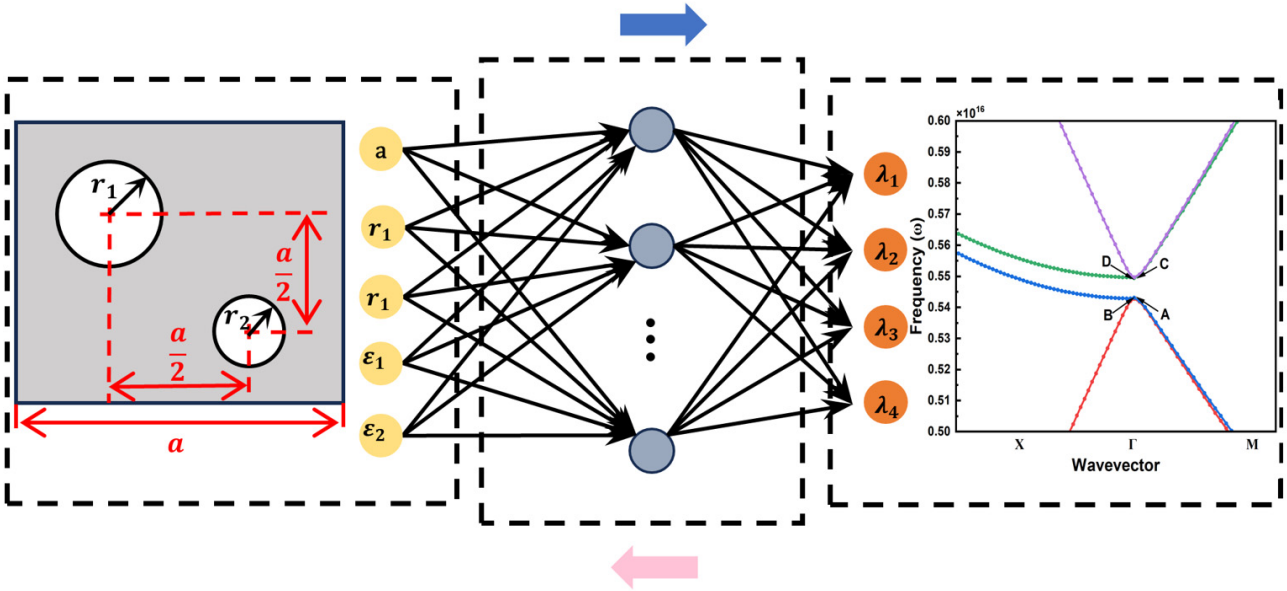

Figure 4. ANN-RBF neural network architecture.

Subsequently, a backpropagation algorithm was used for parameter inverse solving. Based on the trained ANN-RBF neural network, we realized the reverse design function of the photonic crystal structure parameters, which could quickly generate optical structures that meet specific resonant wavelength requirements. A comparison between the predicted and actual lattice constants from the test and training sets in some of the raw data is shown in Figure 5a,b. For the evaluation factors predicted by the ANN-RBF model, we additionally focused on the lattice constant. MAE (Mean Absolute Error), RMSE (Root Mean Square Error), and MARE (Mean Absolute Percentage Error) are three commonly used metrics for measuring prediction errors. MAE reflects the average level of absolute error between predicted and true values and is not sensitive to outliers; a smaller value indicates more accurate predictions. RMSE amplifies the impact of larger errors through squaring, often used to emphasize the penalty for significant errors, and its value shares the same unit as the original data. MARE (also known as MAPE) expresses relative error in percentage form, making it suitable for comparing data of different magnitudes, but it is sensitive to

true values close to zero. The calculation formulas are as follows (where Image is the true value, Image is the predicted value, and Image is the sample size):

$$MAE = \frac{1}{n}\sum_{i=1}^{n}|y_i - \hat{y}_i| \quad (5)$$

$$RMSE = \sqrt{\frac{1}{n}\sum_{i=1}^{n}(y_i - \hat{y}_i)^2} \quad (6)$$

$$MARE = \frac{100\%}{n}\sum_{i=1}^{n}\frac{\left|y_i - \hat{y}_i\right|}{|y_i|} \quad (7)$$

where y_i is the true value, $\hat{y}_i$ is the predicted value, and n is the sample size. The mean absolute error (MAE) of the test set was 0.7610 nm, root mean square error (RMSE) was 1.143×10^{-3} nm, and mean absolute relative error (MARE) was 5.489×10^{-3}. Furthermore, the prediction results of RBF were compared with those of the back propagation algorithm (BP) and extreme learning machine (ELM). BP, as a classical neural network training method, realizes parameter optimization based on gradient descent and chain rule [37,38], which adopts a single hidden layer feedforward neural network structure, and realizes rapid training by randomly initializing the input weights and combining them with the analytical calculation of the output weights [39,40]. As shown in Figure 5c–e, the prediction accuracy of the RBF is significantly better than that of the above two conventional algorithms. The core advantage of RBF is that it can capture the nonlinear effect of small changes in the photonic crystal parameters on the band structure by locally nonlinear mapping of the input space through distance measures, and each hidden layer node corresponds to a local response center.

For verification, we used a double-lattice photonic crystal with a target resonant wavelength of 280 nm. We fixed the first resonant wavelength parameter in the output vector at 280 nm and set reasonable value ranges and scanning steps for the other three resonant wavelength parameters. The system traversed all possible resonant wavelength parameter combinations within a specified range and performed inverse prediction based on a trained RBF neural network to obtain the corresponding double-lattice structure parameter combinations. After eliminating the parameter combination models with nonphysical meanings, we obtained 12 groups of double-lattice photonic crystal structures with resonant wavelengths of 280 nm, as shown in Table 2. It is worth emphasizing that this method can generate multiple combinations of dielectric constants for a single target wavelength, effectively adapting to different epitaxial structure designs of the lasers. Specifically, it refers to the effective refractive index (f) and confinement factor of the photonic crystal layer (Γ_{pc}) applicable to different epitaxial structures. We further calculated the band structure of the predicted photonic crystal using the plane wave expansion method to verify the reliability of the inverse design method. For the group where the air holes exceed the range of the photonic crystal unit cell, the excess parts were removed during the simulation process. The verification results are shown in Figure 6. The MSE between the predicted resonant wavelength of the structure and the target value was 0.3593 nm^2.

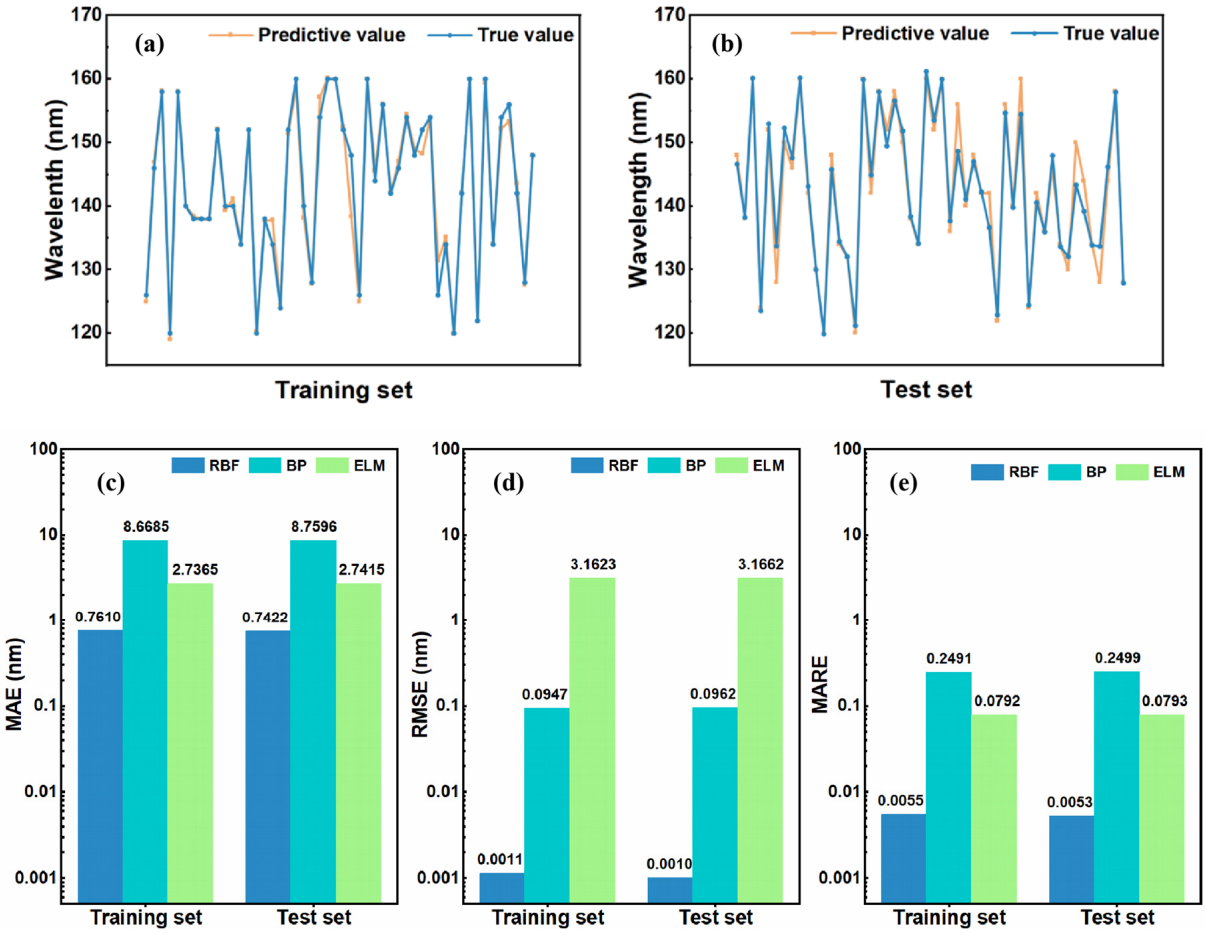

Figure 5. Comparison between predicted and actual lattice constants in (**a**) test sets, (**b**) training sets. Comparison of evaluation metrics for different predictive models using (**c**) MSE, (**d**) RMSE, and (**e**) MARE.

Table 2. Prediction of the double-lattice photonic crystal structures resonant at 280 nm.

Order Number	a (nm)	r_1(nm)	r_2(nm)	ε_a	ε_b	Γ_{pc}(%)	n_{eff}
1	124.78	37.59	34.78	2.1702	2.2992	10.11	2.2352
2	125.21	34.09	36.45	2.1603	2.2894	10.07	2.2227
3	125.69	30.26	38.54	2.1493	2.2787	10.04	2.2085
4	125.78	30.65	44.08	2.1354	2.2801	11.21	2.2095
5	126.21	26.35	40.81	2.1377	2.2674	10.02	2.1936
6	126.74	22.57	43.05	2.1257	2.2558	10.00	2.1794
7	130.21	29.66	26.46	2.0421	2.1769	9.97	2.0825
8	130.4	27.66	28.02	2.0385	2.1732	9.95	2.0779
9	130.53	16.66	39.14	2.0380	2.1721	9.9	2.0807
10	130.53	25.10	30.34	2.0362	2.1708	9.93	2.0756
11	130.59	22.25	33.14	2.0353	2.1698	9.92	2.0756
12	130.59	19.36	36.15	2.0359	2.1702	9.91	2.0773

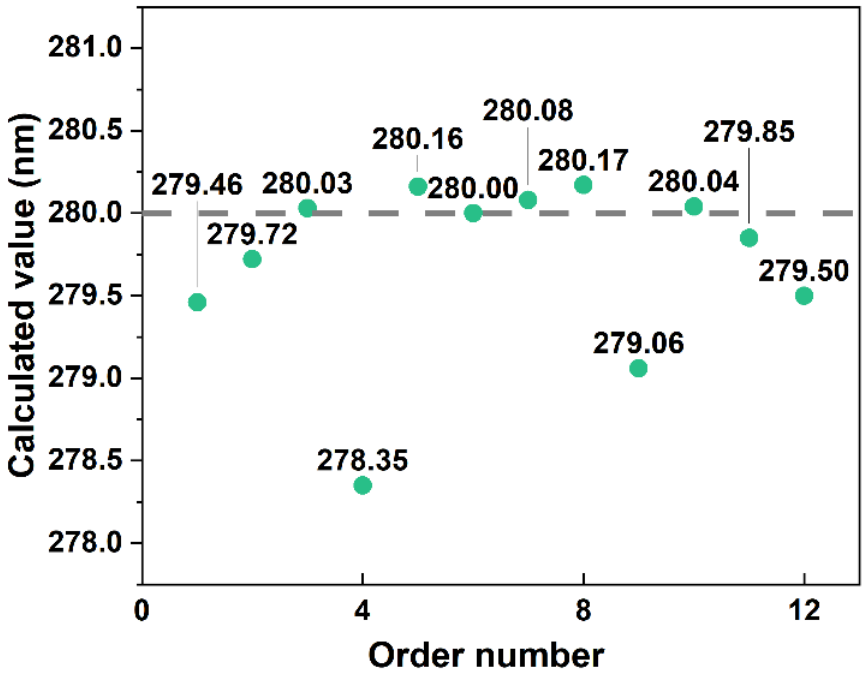

Figure 6. Verification of Predicted Photonic Crystal Band Structures Using PWE.

4. Conclusions

We have proposed a neural network-based approach for the rapid optimization of parameters in the design of deep ultraviolet double-lattice photonic crystals. In these structures, the lattice constant is a critical factor that influences their resonant wavelength, with the random forest algorithm indicating an importance score of 95.24%. Using a target wavelength of 280 nm as an example, we employed the plane wave expansion method to validate the photonic crystal structure designed by our neural network. We successfully designed thirteen photonic crystals that conform to various epitaxial structures, achieving a mean squared error (MSE) of 0.6188 nm^2. These results demonstrate that the ANN-RBF algorithm is reliable for designing photonic crystal microcavities and facilitates rapid iterations in developing surface-emitting lasers based on photonic crystals. Furthermore, this work can be extended to various wavelength bands and epitaxial structures relevant to GaN-based devices.

Author Contributions: Conceptualization, B.Z.; Methodology, M.Z.; Software, B.Z. and L.L.; Validation, J.B. and S.J.; Investigation, J.B., Z.G. and B.H.; Data curation, J.B.; Writing—original draft, B.Z. and X.C.; Writing—review & editing, B.Z. and M.Z. All authors have read and agreed to the published version of the manuscript.

Funding: This research was funded by XJTU Research Fund for Al Science, grant number No. 2025YXYC004 and National Natural Science Foundation of China, grant number No. 61905191.

Data Availability Statement: The original contributions presented in this study are included in the article. Further inquiries can be directed to the corresponding author.

Conflicts of Interest: The authors declare no conflicts of interest.

References

1. Rehman, H.U.; Bi, W.; Rahman, N.U.; Haq, I.; Ullah, I.; Wang, F.; Liu, Y. A Review of Challenges, Solutions, and Improvements in the Performance of Deep Ultraviolet Semiconductor Laser Diodes (DUV LDs). *ACS Appl. Electron. Mater.* **2024**, *6*, 8710–8724. [CrossRef]

2. Chang, H.M.; Gandrothula, S.; Gee, S.; Tak, T.; Wong, M.; Palmquist, N.; Zhang, J.; Trageser, E.; Li, X.; Quevedo, A.; et al. InGaN/GaN edge emitting laser diodes using an epitaxial lateral overgrowth with a low-defect density area of more than 75%. *Jpn. J. Appl. Phys.* **2025**, *64*, 010903. [CrossRef]
3. Fukamachi, T.; Nishinaka, J.; Naniwae, K.; Usuda, S.; Fukai, H.; Sugitani, A.; Uemukai, M.; Tanikawa, T.; Katayama, R. Detuning dependence in current-light-output characteristics of GaN-based DFB laser diodes. *Jpn. J. Appl. Phys.* **2025**, *64*, 022001. [CrossRef]
4. Liu, J.L.; Zhao, F.Y.; Tang, Z.T.; Zhang, X.H.; Ren, A.B.; Wu, J. Advances in high-power vertical-cavity surface-emitting lasers. *J. Phys. D-Appl. Phys.* **2024**, *57*, 353001. [CrossRef]
5. Chang, J.; Chen, D.; Yang, L.; Liu, Y.; Dong, K.; Lu, H.; Zhang, R.; Zheng, Y. High-Quality Crystal Growth and Characteristics of AlGaN-Based Solar-Blind Distributed Bragg Reflectors with a Tri-layer Period Structure. *Sci. Rep.* **2016**, *6*, 29571. [CrossRef]
6. Yoshida, M.; De Zoysa, M.; Ishizaki, K.; Kunishi, W.; Inoue, T.; Izumi, K.; Hatsuda, R.; Noda, S. Photonic-crystal lasers with high-quality narrow-divergence symmetric beams and their application to LiDAR. *J. Phys. Photonics* **2021**, *3*, 022006. [CrossRef]
7. Hong, Y.H.; Miao, W.C.; Hsu, W.C.; Hong, K.B.; Lin, C.L.; Lin, C.; Chen, S.C.; Kuo, H.C. Progress of Photonic-Crystal Surface-Emitting Lasers: A Paradigm Shift in LiDAR Application. *Crystals* **2022**, *12*, 800. [CrossRef]
8. Liu, J.S.; Song, Y.; Chen, Y.Y.; Qin, L.; Liang, L.; Niu, S.; Wang, Y.; Jia, P.; Qiu, C.; Lei, Y.X.; et al. Research Progress of Horizontal Cavity Surface-Emitting Laser. *Sensors* **2023**, *23*, 5021. [CrossRef]
9. Imada, M.; Noda, S.; Chutinan, A.; Tokuda, T.; Murata, M.; Sasaki, G. Coherent two-dimensional lasing action in surface-emitting laser with triangular-lattice photonic crystal structure. *Appl. Phys. Lett.* **1999**, *75*, 316–318. [CrossRef]
10. Lu, H.Y.; Tian, S.C.; Tong, C.Z.; Wang, L.J.; Rong, J.M.; Liu, C.Y.; Wang, H.; Shu, S.L.; Wang, L.J. Extracting more light for vertical emission: High power continuous wave operation of 1.3-mum quantum-dot photonic-crystal surface-emitting laser based on a flat band. *Light. Sci. Appl.* **2019**, *8*, 108. [CrossRef]
11. Yoshida, M.; De Zoysa, M.; Ishizaki, K.; Tanaka, Y.; Kawasaki, M.; Hatsuda, R.; Song, B.; Gelleta, J.; Noda, S. Double-lattice photonic-crystal resonators enabling high-brightness semiconductor lasers with symmetric narrow-divergence beams. *Nat. Mater.* **2019**, *18*, 121–128. [CrossRef]
12. Shao, Z.K.; Chen, H.Z.; Wang, S.; Mao, X.R.; Yang, Z.Q.; Wang, S.L.; Wang, X.X.; Hu, X.; Ma, R.M. A high-performance topological bulk laser based on band-inversion-induced reflection. *Nat. Nanotechnol.* **2019**, *15*, 67–72. [CrossRef]
13. Taguchi, N.; Iwai, A.; Noguchi, M.; Takahashi, H.; Michiue, A.; De Zoysa, M.; Inoue, T.; Ishizaki, K.; Noda, S. Green-wavelength GaN-based photonic-crystal surface-emitting lasers. *Appl. Phys. Express* **2024**, *17*, 012002. [CrossRef]
14. Masahiro, Y.; Shumpei, K.; Takuya, I.; John, G.; Koki, I.; Menaka, D.Z.; Kenji, I.; Susumu, N. High-brightness scalable continuous-wave single-mode photonic-crystal laser. *Nature* **2023**, *618*, 727–732.
15. De Zoysa, M.; Yoshida, M.; Song, B.; Ishizaki, K.; Inoue, T.; Katsuno, S.; Izumi, K.; Tanaka, Y.; Hatsuda, R.; Gelleta, J.; et al. Thermal management for CW operation of large-area double-lattice photonic-crystal lasers. *J. Opt. Soc. Am. B* **2020**, *37*, 3882–3887. [CrossRef]
16. Inoue, T.; Yoshida, M.; Gelleta, J.; Izumi, K.; Yoshida, K.; Ishizaki, K.; De Zoysa, M.; Noda, S. General recipe to realize photonic-crystal surface-emitting lasers with 100-W-to-1-kW single-mode operation. *Nat. Commun.* **2022**, *13*, 3262. [CrossRef]
17. Yoshida, M.; Kawasaki, M.; Zoysa, M.D.; Ishizaki, K.; Inoue, T.; Tanaka, Y.; Hatsuda, R.; Noda, S. Experimental Investigation of Lasing Modes in Double-Lattice Photonic-Crystal Resonators and Introduction of In-Plane Heterostructures. *Proc. IEEE* **2020**, *108*, 819–826. [CrossRef]
18. Itoh, Y.; Kono, N.; Fujii, K.; Yoshinaga, H.; Fujiwara, N.; Ogasawara, M.; Tanaka, R.; Yagi, H.; Yanagisawa, M.; Yoshida, M.; et al. High-power with single-lobe beam of 1.3-μm InP-based double-lattice photonic-crystal surface-emitting lasers. *Proc. SPIE* **2023**, *12440*, 6.
19. Itoh, Y.; Kono, N.; Inoue, D.; Fujiwara, N.; Ogasawara, M.; Fujii, K.; Yoshinaga, H.; Yagi, H.; Yanagisawa, M.; Yoshida, M.; et al. High-power CW oscillation of 1.3-μm wavelength InP-based photonic-crystal surface-emitting lasers. *Opt. Express* **2022**, *30*, 29539–29545. [CrossRef]
20. Itoh, Y.; Aoki, T.; Fujii, K.; Yoshinaga, H.; Fujiwara, N.; Takada, K.; Ogasawara, M.; Sawada, Y.; Yagi, H.; Yanagisawa, M.; et al. High-power and high-efficiency operation of 1.3 microm-wavelength InP-based photonic-crystal surface-emitting lasers with metal reflector. *Opt. Express* **2024**, *32*, 12520–12527. [CrossRef]
21. Aoki, T.; Itoh, Y.; Fujii, K.; Yoshinaga, H.; Fujiwara, N.; Ogasawara, M.; Sawada, Y.; Tanaka, R.; Yagi, H.; Yanagisawa, M.; et al. High-power, stable single-mode CW operation of 1550 nm wavelength InP-based photonic-crystal surface-emitting lasers. *Appl. Phys. Express* **2024**, *17*, 042004. [CrossRef]
22. Itoh, Y.; Aoki, T.; Fujii, K.; Yoshinaga, H.; Fujiwara, N.; Ogasawara, M.; Sawada, Y.; Tanaka, R.; Machinaga, K.; Yagi, H.; et al. Power Scalability of 1.55-μm-Wavelength InP-Based Double-Lattice Photonic-Crystal Surface-Emitting Lasers With Stable Continuous-Wave Single-Mode Lasing. *IEEE J. Sel. Top. Quantum Electron.* **2025**, *31*, 1700408. [CrossRef]
23. Molesky, S.; Lin, Z.; Piggott, A.Y.; Jin, W.; Vucković, J.; Rodriguez, A.W. Inverse design in nanophotonics. *Nat. Photonics* **2018**, *12*, 659–670. [CrossRef]

24. Wiecha, P.R.; Arbouet, A.; Girard, C.; Muskens, O.L. Deep learning in nano-photonics: Inverse design and beyond. *Photonics Res.* **2021**, *9*, B182–B200. [CrossRef]
25. Kazanskiy, N.L.; Oseledets, I.V.; Nikonorov, A.V.; Chertykovtseva, V.O.; Khonina, S.N. Exploring the Frontier of Integrated Photonic Logic Gates: Breakthrough Designs and Promising Applications. *Technologies* **2025**, *13*, 314. [CrossRef]
26. Wurzberger, F.; Schwenker, F. Learning in Deep Radial Basis Function Networks. *Entropy* **2024**, *26*, 368. [CrossRef]
27. Hamedi, S.; Jahromi, H.D. Performance analysis of all-optical logical gate using artificial neural network. *Expert Syst. Appl.* **2021**, *178*, 115029. [CrossRef]
28. Jiang, J.Q.; Chen, M.K.; Fan, J.A. Deep neural networks for the evaluation and design of photonic devices. *Nat. Rev. Mater.* **2021**, *6*, 679–700. [CrossRef]
29. Noda, S.; Yokoyama, M.; Imada, M.; Chutinan, A.; Mochizuki, M. Polarization Mode Control of Two-Dimensional Photonic Crystal Laser by Unit Cell Structure Design. *Science* **2001**, *293*, 1123–1125. [CrossRef] [PubMed]
30. Imada, M.; Chutinan, A.; Noda, S.; Mochizuki, M. Multidirectionally distributed feedback photonic crystal lasers. *Phys. Rev. B* **2002**, *65*, 195306. [CrossRef]
31. Wang, Z.Y.; Wang, P.Y.; Lu, H.Y.; Meng, B.; Wang, Y.J.; Tong, C.Z.; Wang, L.J. Symmetry Criterion and Far-Field Control of Photonic-Crystal Surface-Emitting Lasers. *Appl. Sci.* **2022**, *12*, 10581. [CrossRef]
32. Sakai, K.; Miyai, E.; Sakaguchi, T.; Ohnishi, D.; Okano, T.; Noda, S. Lasing band-edge identification for a surface-emitting photonic crystal laser. *IEEE J. Sel. Areas Commun.* **2005**, *23*, 1335–1340. [CrossRef]
33. Plihal, M.; Shambrook, A.; Maradudin, A.A.; Sheng, P. Two-dimensional photonic band structures. *Opt. Commun.* **1991**, *80*, 199–204. [CrossRef]
34. Breiman, L. Random forests. *Mach. Learn.* **2001**, *45*, 5–32. [CrossRef]
35. Wu, Y.; Wang, Y.G.; Liu, H.B.; Xie, L.P.; Jiao, L.L.; Lu, P.Z. Risk assessment of bridge construction investigated using random forest algorithm. *Sci. Rep.* **2024**, *14*, 20964. [CrossRef]
36. Biau, G.; Scornet, E. A random forest guided tour. *Test* **2016**, *25*, 197–227. [CrossRef]
37. Rumelhart, D.E.; Hinton, G.E.; Williams, R.J. Learning Representations by Back Propagating Errors. *Nature* **1986**, *323*, 533–536. [CrossRef]
38. LeCun, Y.; Bengio, Y.; Hinton, G. Deep learning. *Nature* **2015**, *521*, 436–444. [CrossRef] [PubMed]
39. Huang, G.B.; Zhu, Q.Y.; Siew, C.K. Extreme learning machine: Theory and applications. *Neurocomputing* **2006**, *70*, 489–501. [CrossRef]
40. Huang, G.B.; Zhou, H.; Ding, X.; Zhang, R. Extreme learning machine for regression and multiclass classification. *IEEE Trans. Syst. Man Cybern. Part B Cybern.* **2012**, *42*, 513–529. [CrossRef]